Highly efficient electrocatalytic CO_2 reduction over pyrolysis–free conjugated metallophthalocyanine networks in full pH range

Qiao Wu [a,b], Duan–Hui Si [b], Jun Liang [b], Yuan–Biao Huang [b,c,d,*], Rong Cao [a,b,c,d,*]

[a] Department of Chemistry, College of Chemistry and Chemical Engineering, Xiamen University, Xiamen 361005, China
[b] State Key Laboratory of Structural Chemistry, Fujian Institute of Research on the Structure of Matter, Chinese Academy of Sciences, Fuzhou 350002, China
[c] University of Chinese Academy of Sciences, Beijing 100049, China
[d] Fujian Science & Technology Innovation Laboratory for Optoelectronic Information of China Fuzhou, Fujian 350108, China

ARTICLE INFO

ABSTRACT

Herein, we report the first work on pyrolysis–free synthesis of robust conjugated metallophthalocyanine–based covalent triazine frameworks (MPc–CTF, M= Co, Ni) for pH-universal electrocatalytic CO_2 reduction reaction (CO_2RR). CoPc–CTF shows high CO Faradaic efficiency over 94%, and long-term stability over 10 h in full pH range, and industry level CO partial current densities of 378.8 mA cm^{-2}, 165.9 mA cm^{-2}, 172.5 mA cm^{-2} in alkaline, neutral and acidic electrolytes, respectively. Particularly, the CO_2 utilization efficiency reaches 51.3% in acidic electrolytes. Moreover, operando characterizations and density functional theory calculations indicate the promoting effect of triazine moiety in CoPc–CTF to accelerate the formation of *COOH intermediates during CO_2RR. This work provides an encouraging direction for designing robust conjugated network supported single site catalysts to access high product selectivity and high carbon utilization efficiency in electrocatalytic CO_2 reduction reaction.

1. Introduction

There has been intense interest in the development of new efficient catalysts for the chemical utilization of C1 gases such as carbon dioxide (CO_2) as feedstock to afford valuable chemicals [1–4]. In this regard, the electrocatalysis of CO_2 reduction reaction (CO_2RR) is promising for various products including carbon monoxide (CO) [5–11], formic acid [12–14], methane [15,16], methanol [17,18], ethylene [19–21] and ethanol [22] under mild conditions. Currently, CO_2RR is mainly operated in near–neutral or alkaline media since hydrogen evolution reaction (HER) has dominated in acidic electrolytes [23–26]. In near–neutral media, $KHCO_3$ electrolyte is usually employed to keep interfacial pH neutral and stable, thus suppressing HER [27]. In alkaline media, the gas diffusion electrode (GDE) is utilized, where gas–liquid–solid interfaces are formed to provide possibility of operating electrolyzers at industrial current densities, and high pH is also advantageous for suppressing HER [28–31]. Nevertheless, the carbonate formation problem obliges continuous refreshment of OH^- electrolytes in a flow cell configuration to achieve high current stability and stable performance in both neutral and alkaline media [32–34]. To address this issue, CO_2 electrolysis in an acidic media offers a viable strategy to avoid carbonate formation and eliminate CO_2 crossover [23,24,35], but remains challenging to simultaneously inhibit HER and promote CO_2RR with high efficiency and selectivity. However, currently, very few catalysts could operate CO_2RR under acidic conditions, and stable heterogeneous frameworks catalyst, that can effectively promote CO_2RR in full pH range, is not yet reported.

Noble metal–based electrocatalysts, such as Pd–, Au–, and Ag–based electrodes are highly selective to produce CO in near–neutral or alkaline media, but limited reserves impede their commercialization [36,37]. Thus, the exploration of highly efficient noble metal–free multifunctional electrocatalysts with high selectivity and high current density values for producing CO are urgently demanded. Metal single–site catalysts (SSC) are being widely investigated for CO_2RR because of their tunable active sites, the maximized atom utilization efficiency, and tunable selectivity towards specific products [38–41]. Nevertheless, most of reported SSC are prepared via high–temperature pyrolysis, which are severely affected by the precise elemental ratio of precursors and the rigorous manipulation of the carbonization process [42,43]. Meanwhile, the metal atoms are prone to migrate and agglomerate to form metal particles.[44,45] The randomly dispersed single active

species via high–temperature pyrolysis approach is unpredictable and difficult to repeat in an atomic manner.[44,45] Therefore, it is highly desirable to develop precisely controllable synthesis method towards robust SSC with high catalytic CO_2RR activity in full pH range.

Porous covalent triazine frameworks (CTFs) are one promising class of conjugated frameworks linked by triazine rings with aromatic N–rich structures, large CO_2 adsorption and remarkable chemical stability [46–51]. Thus, CTFs can be ideal platforms to support highly dispersed metal single–sites for CO_2RR when functional macrocycles such as metal phthalocyanines are integrated into the backbones. It is known that phthalocyanine unit can provide two pyrrolic and two pyridinic nitrogen atoms to firmly trap metal atoms [52,53]. Nevertheless, most CTF–based materials are obtained via ionothermal synthesis accompanied with pyrolysis under high temperatures, which led to unpredictable structures [39]. Thus, we try to explore pyrolysis–free approaches for the preparation of stable metallophthalocyanine–based CTF electrocatalysts by the polymerization of rationally designed metallophthalocyanine with carbonitrile groups under mild conditions for CO_2RR in various electrolytes.

Herein, for the first time, we prepared the electrocatalysts with co-ordination dispersion of metal atoms on conjugated metal-lophthalocyanine CTF polymers (termed as MPc–CTF, M = Co, Ni) (Scheme 1) via mild pyrolysis–free synthesis approach, aimed at enhancing CO_2RR performance in a full pH range. Benefiting from the abundant Co–N$_4$ single sites, functional triazine groups, large CO_2 adsorption capability, good conductivity and stable conjugated frameworks, the resultant triazine functionalized CoPc–CTF catalysts exhibit improved CO_2RR performance in a full pH range with the J_{CO} value reaching an industrial–level current density values of 378.8 mA cm^{-2} at −1.0 V versus the reversible hydrogen electrode (vs. RHE) in 1 M KOH (pH = 13.4), and J_{CO} of 172.5 mA cm^{-2} at −1.5 V in phosphoric acid electrolyte (pH = 2). Moreover, the high FE$_{CO}$ can reach 99.2% after 10 h catalysis at −0.6 V in 1 M KOH. CoPc–CTF is also capable of delivering stable current densities of 150.0 mA cm^{-2} with FE$_{CO}$ over 93.2% after 10 h durability test in phosphoric acid. To further understand the catalytic process on CoPc−CTF, the experimental comparisons and theoretical DFT calculations reveal that the triazine unit in CoPC–CTF is favor of lowered energy barriers in CO_2RR process, thus leading to enhanced electrocatalysis of CO generation.

2. Experimental Section

2.1. Reagents and Chemicals

All reagents were purchased from commercial sources without further purification. 2,4–dichlorobenzonitrile, 1,1′–Bis(diphenylphosphino)ferrocene, 1,8 diazabicyclo(5,4)undecane, 4–Dimethylamino pyridine, Zn(CN)$_2$, Zinc, and trifluoromethanesulfonic acid were purchased from Adamas. Before using, zinc was stirred with 1 M HCl

aqueous solution, filtered and washed thoroughly with water, acetone and diethyl ether, and dried under vacuum at room temperature.

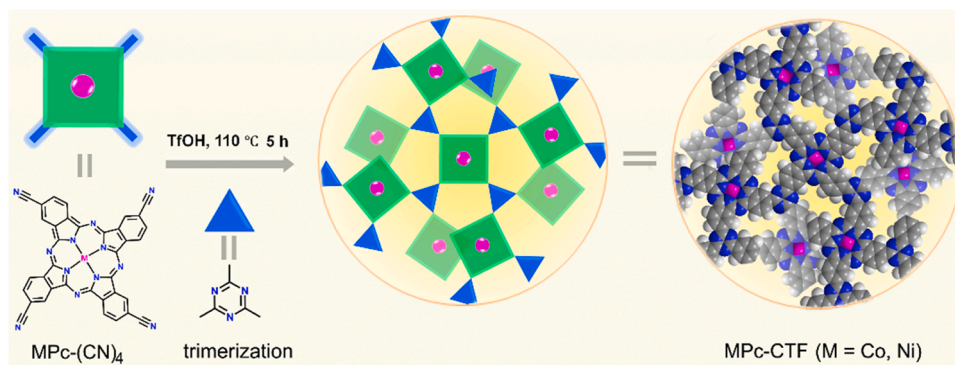### 2.2. Synthesis of metal tetracyanophthalocyanine [MPc–(CN)$_4$] (M = Co, Ni)

CoPc–(CN)$_4$ was prepared using a modified method from the literature [54]. To a 50 mL round bottom flask fitted with a condenser, 10 mL DMF was added and heated to 110 °C, while being degassed with N$_2$ under stirring. Co(CH$_3$COO)$_2$·4 H$_2$O (149.4 mg, 0.60 mmol) was then added, followed by benzene–1,2,4–tricarbonitrile (188.6 mg, 1.20 mmol). The whole mixture was then heated up to 140 °C to be blue in color. Then 1,8 diazabicyclo(5,4)undecene (DBU, 0.8 mL, 5.25 mmol) was added and the reaction turned a maroon color. 40 min after reaching at 140 °C, another batch of DBU (0.3 mL, 1.97 mmol) was added and kept for 5 h. The reaction was poured into 80 mL water, and was left still overnight. The suspension was filtered, washed with 200 mL water. The solid was then stirred in a 0.5 M HCl solution, then filtered and washed with copious water, then stirred in 0.5 M NaOH, then vacuum filtered. Again, the solid was stirred in 0.5 M HCl solution and then treated again with 0.5 M NaOH, filtered, and washed with copious water, then dried under vacuum over night at 70 °C. NiPc–(CN)$_4$ was synthesized under similar conditions of CoPc–(CN)$_4$ with NiCl$_2$·6 H$_2$O instead of Co(CH$_3$COO)$_2$·4 H$_2$O as the metal source.

2.3. Synthesis of MPc–CTF (M = Co, Ni)

CoPc–CTF was prepared using a modified method from the literature [48]. CoPc–(CN)$_4$ (50 mg, 0.075 mmol) was added into a 10 mL glass reaction vessel under N$_2$ atmosphere at –10 °C. Tri-fluoromethanesulfonic acid (1.5 mL, 16.80 mmol) was then added into the solution dropwise. The mixture was stirred at –10 °C for 1 h, then transferred to an oil bath at 110 °C and kept for 5 h under stirring. The suspension was grinded carefully and washed with 0.1 M ammonia solution until neutral. The powder was washed with water, ethanol, acetone and THF and finally dried under vacuum over night at 70 °C. NiPc–CTF was prepared from NiPc–(CN)$_4$ under similar conditions as that of CoPc–CTF from CoPc–(CN)$_4$.

2.4. Characterization

FT–IR were recorded on a PerkinElmer Spectrum One. SEM images were recorded by a FEIT 20 working at 10 KV. TEM images were taken on a FEI TECNAI G2 F20 microscope equipped with EDS detector at an accelerating voltage of 200 kV. CO_2 sorption isotherms were measured on Micrometrics ASAP 2020. Metal content were detected by ICP on an Ultima2 analyzer (Jobin Yvon). XPS measurements were performed on an ESCALAB 250Xi (Thermo Fisher) using an Al Ka source (15 kV, 10 mA). Raman spectra were recorded on a Labram HR Evolution

Scheme 1. Schematic illustration of the pyrolysis–free synthesis of conjugated metallophthalocyanine networks MPc–CTF (M = Co, Ni).

microscope with a laser excitation wavelength at 633 nm. Ex-situ UV–Vis spectra (Fig. 1b and Fig. S9b) were recorded on Shimadzu UV–2600. We tested ex-situ Raman spectra (Fig. S6) of fresh samples, and the in-situ Raman spectra (Fig. S28) of CoPc-CTF during electrolysis processes. ^{1}H NMR and ^{13}C NMR spectra was performed at AVANCE III BrukerBiospin spectrometer at 400 MHz. ATR–FTIR was obtained on a Nicolet 6700 (Thermo Fisher). XAFS measurment and data analysis: XAFS spectra at the metal K–edge was collected at BL14W1 station in Shanghai Synchrotron Radiation Facility (SSRF).

2.5. Electrochemical measurements

2.5.1. CO₂ Reduction in H–type cell

The electrochemical measurements were performed in a airtight H–type cell with two–compartments separated by a Nafion–117 membrane at room temperature, each compartment contained 70 mL electrolyte (0.5 M KHCO₃ aqueous solution). All electrochemical tests were conducted on the CHI140C workstation. A typical three–electrode system was employed, using carbon paper electrode as the working electrode, platinum gauze as counter electrodes, Ag/AgCl electrode in saturated KCl solution as reference electrodes. Typically, the 5 mg catalyst and 2 mg Ketjenblack (ECP600JD) were dispersed in 960 μL of isopropanol and 40 μL of Nafion binder solution (5 wt%) under sonication for 1 h to form a homogeneous ink. Then 400 ug of the catalyst was loaded onto the carbon paper electrode (CeTech GDL280) with 1×1 cm². During the electrochemical measurements, linear sweep voltammetry (LSV) with a scan rate of 10 mV s⁻¹ was carried out in Ar–saturated 0.5 M KHCO₃ solution (pH = 8.5) or in CO₂–saturated 0.5 M KHCO₃ solution (pH = 7.2). The CO₂ flow was kept constant at 30 sccm using a mass flow controller. The gas phase composition was analyzed by gas chromatograph (Agilent 7820 A). The separated gas products were analyzed by a thermal conductivity detector (for H₂) and a flame ionization detector (for CO). The liquid products were analyzed afterwards by quantitative nuclear magnetic resonance (Bruker ECZ400S) using dimethyl sulphoxide (DMSO) as an internal standard. Solvent presaturation technique was implemented to suppress the water peak.

2.5.2. CO₂ Reduction in Flow cell

Alkaline media: Electrochemical Measurements at high current densities was performed in a four–part flow cell using constant potential electrolysis method. The flow cell contained a gas–diffusion layer (GDL, Sigracet 29 BC), an anion exchange membrane (fumasep FAB–PK–130), a platinum foil (1.0 ×3.0 cm²) anode, and an Ag/AgCl electrode. The working electrodes were prepared by drop–casting catalyst ink onto the GDL to reach a total mass loading of ~1 mg cm⁻². Cathode and anode are respectively connected with copper tape (current collector). Prior to the electrochemical tests, the electrolytes (1 M KOH) were separately circulated compartments using peristaltic pumps at flow rates of 10 mL min⁻¹. The flow–out electrolyte was directly collected for product analysis or transferred to waste bottle instead of feeding back to the cell in order to eliminate pH drop induced by neutralization reaction between KOH and CO₂. CO₂ gas was directly fed to the cathodic GDE at a rate of 25 sccm. All the electrode potentials were measured against the Ag/AgCl electrode without iR compensation and measured potentials were converted to reversible hydrogen electrode (RHE) scale.

Acid media: The flow cell contained a gas–diffusion layer, cation exchange membrane (Nafion–117), iridium oxide supported titanium (IrOₓ–Ti) electrodes (1.0 ×3.0 cm²), and an Ag/AgCl electrode. The catalyst loading of ~1 mg cm⁻². The phosphoric acid electrolyte (0.5 M H₃PO₄, 0.5 M KH₂PO₄, and 1.5 M KCl, pH = 2) as the catholyte, 0.5 M H₂SO₄ as the anolyte. The electrolytes were separately circulated compartments using circulating peristaltic pumps at flow rates of 5 mL min⁻¹. CO₂ gas was directly fed to the cathodic GDE at a rate of 20 sccm. All the electrode potentials were measured against the Ag/AgCl electrode without iR compensation and measured potentials were

converted to reversible hydrogen electrode (RHE) scale.

The Faraday efficiency of a certain gas product was calculated based on the following equations:

$$FE = \frac{PV}{TR} \times \frac{v NF \times 10^{-6} (m^3/mL)}{I \times 60 (s/min)} \tag{1}$$

Where v (vol%) is volume concentration of certain gas product in the exhaust gas from the cell (GC data); V is gas flow rate measured by a flow meter, 30 mL min⁻¹; I is total steady–state cell current; N is the electron transfer number for product formation; F is Faradaic constant, 96485 C mol⁻¹; R is universal gas constant, 8.314 J mol⁻¹ K⁻¹; P: is one atmosphere, 1.013×10^5 Pa; T is room temperature, 298.15 K.

3. Results and discussion

3.1. Structural analysis of the catalysts

As shown in Scheme 1, the conjugated metallophthalocyanine–based MPc–CTF (M = Co, Ni) were synthesized by the facile trimerization reaction of metal tetracyanophthalocyanine [MPc–(CN)₄, M = Co, Ni] catalyzed by trifluoromethanesulfonic acid (TfOH) as a solvent at 110 °C for 5 h (Scheme S1-S3, Fig. S1–S4). It should be noted that the MPc–(CN)₄ monomer can be dissolved in TfOH, and can maintain the M–N₄ structure under this condition [54,55]. Compared to the trimerization reaction under molten zinc chloride at high temperatures usually above 400 °C [39,46,47], the organic acid (e.g., TfOH) catalyzed polymerization method used herein has the advantages of short heating time and absence of carbonization to avoid the destruction of M–N₄ structure (Scheme 1). Notably, this is the first time to prepare CTFs containing metals using the TfOH catalyzed pyrolysis–free method. In principle, the 3D conjugated triazine frameworks can be formed due to the use of conjugated monomers and expected 3,4–connectivity networks. The Fourier transform infrared spectroscopy (FT–IR) tests revealed that the characteristic triazine units stretching vibration bands at 1664 cm⁻¹ and 1384 cm⁻¹ were observed (Fig. 1a), while the stretching band at 2225 cm⁻¹ attributed to carbonitrile groups of CoPc–(CN)₄ monomers disappeared after the polymerization, indicating the completion of the trimerization reaction [56]. The UV–Vis spectra of both the CoPc–(CN)₄ and CoPc–CTF showed the typical Q–band in the visible region (600–800 nm) and the B–band in the ultraviolet region (300–400 nm) of metallophthalocyanine (Fig. 1b) [57], suggesting the intact CoPc unit structure of CoPc–CTF. Compared with the CoPc–(CN)₄ monomer, the Q–band of CoPc–CTF was slightly red–shifted to about 10 nm, which were probably caused by the formation of conjugated metal-lophthalocyanine–based networks linked by aromatic triazine [57]. The solid–state ^{13}C NMR (ss ^{13}C NMR) spectrum of CoPc–CTF shows a peak (Fig. S5) at 167.9 ppm, which is assignable to the carbons in triazine rings [58,59]. The Raman spectrum of CoPc–CTF shows several typical bands of CoPc–(CN)₄ monomer at 686, 749, 1120, 1320, 1459, and 1536 cm⁻¹ (Fig. S6a), which proves that CoPc–CTF has the basic skeleton of a phthalocyanine [53,60]. The peaks at 686 and 972 cm⁻¹ belong to the triazine ring in CoPc–CTF, which are partially overlapped with the peaks of the phthalocyanine ring [61,62], while the peak's intensity of CoPc–CTF is stronger than that of CoPc–(CN)₄, which confirmed the successful trimerization reaction in CoPc–CTF. Based on the analyses results of FT–IR, UV–vis, ss ^{13}C NMR spectrum and Raman spectrum, these results confirmed the successful condensation reaction required for the CoPc–CTF structure.

The morphology of the typical CoPc–CTF catalyst was investigated by scanning electron microscopy (SEM) and transmission electron microscopy (TEM). The SEM image of CoPc–CTF showed the nano-structures morphology (Fig. 1c). The TEM image in Fig. 1d confirmed the nanostructures and excluded the formation of Co particles. The aberration–corrected high–angle annular dark–field scanning transmission electron microscope (AC–HAADF–STEM) image further
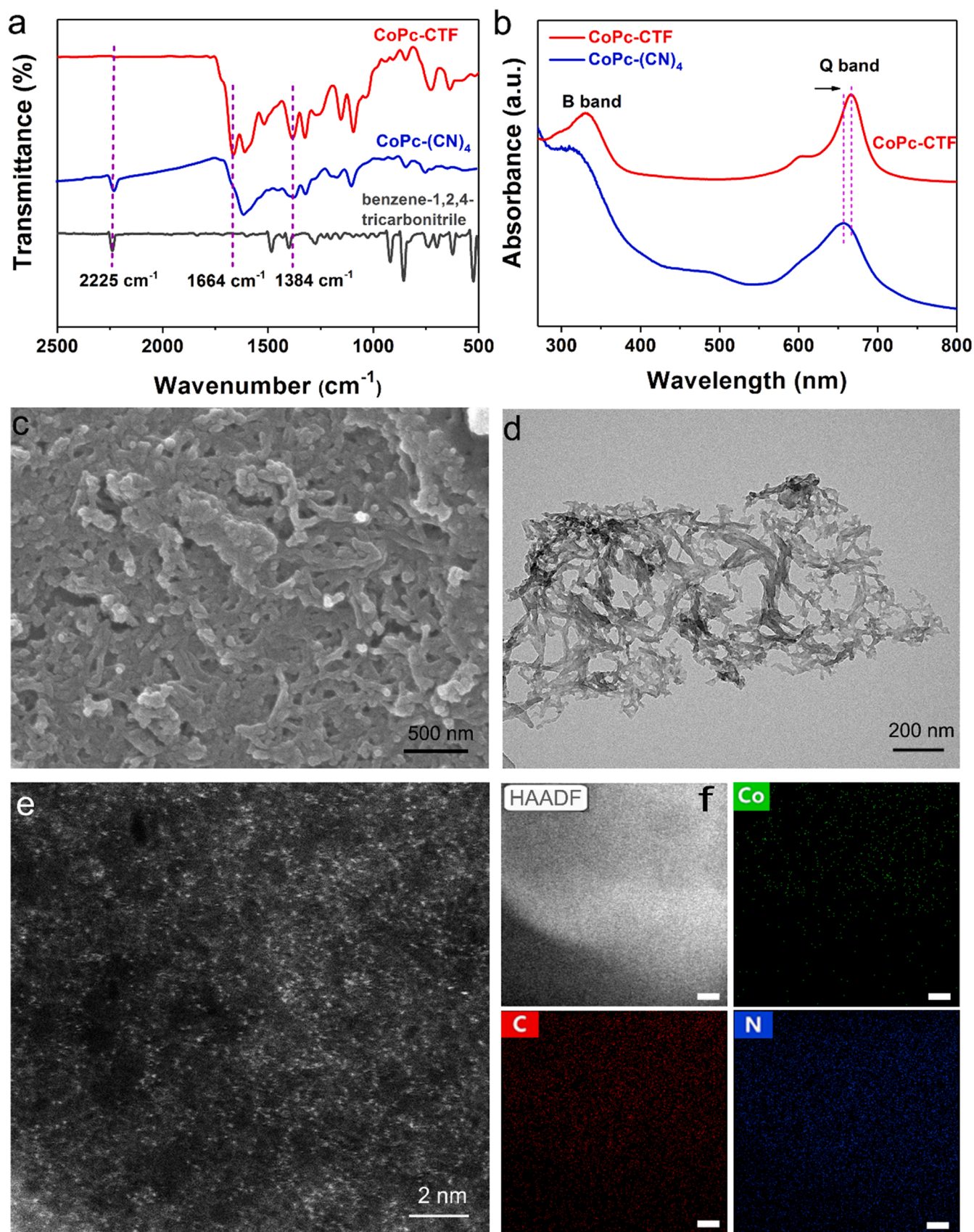
Fig. 1. Structural characterization of CoPc–CTF. (a) FT–IR spectra, and (b) UV–Vis spectra of CoPc–(CN)$_4$ and CoPc–CTF. (c) SEM image, (d) TEM image, (e) AC–HAADF–STEM image and (f) the elemental mapping of CoPc–CTF (Co, green; C, red; N, blue), scale bar: 5 nm.

revealed that a plentiful of bright spots assigned to the atomic level of Co sites were well dispersed in the networks of CoPc–CTF (Fig. 1e). Moreover, the corresponding elemental mapping images (Fig. 1f) demonstrated that Co, C, N element were homogeneously distributed throughout the nanobelt structures of CoPc–CTF material, suggesting Co species was in an atomically dispersed form. Such highly dispersed abundant Co single active sites could facilitate the electrocatalytic CO_2RR performance. The CO_2 adsorption isotherm of CoPc–CTF was collected to show moderate CO_2 uptake capacity with a value of 17 cm³ g⁻¹ at 273 K under 1 bar (Fig. S7). The hysteresis desorption curve indicated the good affinity of nitrogen–rich CoPc–CTF networks towards CO_2, which should be beneficial for promoting the electrocatalytic CO_2RR.

The inductively coupled plasma atomic emission spectroscopy (ICP–AES) demonstrated that the CoPc–CTF catalyst had a high Co content of 5.05 wt% (Table S1). The X–ray photoelectron spectroscopy (XPS) spectra of Co 2p in CoPc–CTF display two peaks at 780.6 eV (Co $2p_{3/2}$) and 796.0 eV (Co $2p_{1/2}$), which indicated the dominance of Co^{2+} centers in CoPc–CTF (Fig. 2a). In order to further investigate the electronic structure and coordination environment of metal active sites in CoPc–CTF, the synchrotron–based X–ray absorption spectroscopy (XAS) test was.

carried out. The X–ray absorption near edge structure (XANES) of Co K–edge shows two fingerprint peaks of Co–N₄ symmetrical structure in CoPc–(CN)₄ monomers and CoPc–CTF (Fig. 2b) [63]. One weak peak at 7710.5 eV is attributed to the dipole forbidden 1 s to 3d transition, and the other at 7716.5 eV can be assigned to the shakedown satellite 1 s to $4p_z$ transition [63,64]. The Co near–edge position of CoPc–CTF is more

close to that of CoPc–(CN)₄ monomers, confirming that the valence state of Co atoms in CoPc–CTF is + 2, which is consistent with the XPS analysis results (Fig. 2a). The coordination environment of Co atoms was further analyzed by extended X–ray absorption fine structure (EXAFS) (Fig. 2c). A major peak at 1.45 Å corresponding to Co–N bond is observed for CoPc–CTF and the CoPc–(CN)₄ monomer, suggesting that the Co centers were coordinated with N atoms. Furthermore, no Co–Co bond at 2.17 Å is observed in CoPc–CTF (Fig. 2c), indicating that the Co centers exist dominantly as atomically isolated Co sites, which is consistent with the aberration–corrected AC–HAADF–STEM results (Fig. 1e). To obtain quantitative structural parameters of the Co atoms, the EXAFS fitting analysis of CoPc–CTF was conducted, which indicates that the average coordination number of Co–N is 4.0 (Fig. 2d and Table S2), which is consistent with CoPc–(CN)₄ monomer, suggesting that the Co phthalocyanines structure in CoPc–CTF is retained (Fig. S8). Thus, the AC–HAADF–STEM images, XPS, and XAS analysis results indicate that CoPc–CTF was obtained as single–site metal catalyst.

To demonstrate the facile synthetic route of MPc–CTF materials by the simple method, we further prepared the NiPc–CTF framework based on NiPc–(CN)₄ monomer for comparison in CO_2RR performance. FT–IR spectroscopy, UV–Vis spectroscopy, and ss ¹³C NMR spectrum analysis of NiPc–CTF revealed that the trimerization reaction was successful (Fig. S9–S10). The Raman spectrum of NiPc–CTF is similar to those of NiPc–(CN)₄ monomer with several typical bands at 687, 748, 1121, 1320, 1456, and 1539 cm⁻¹ (Fig. S6b), which demonstrates that NiPc–CTF possesses the basic skeleton of a phthalocyanine [53,60]. The triazine ring characteristic peak at 687 and 968 cm⁻¹ in NiPc–CTF were observed [61,62], which confirmed the successful synthesis of the
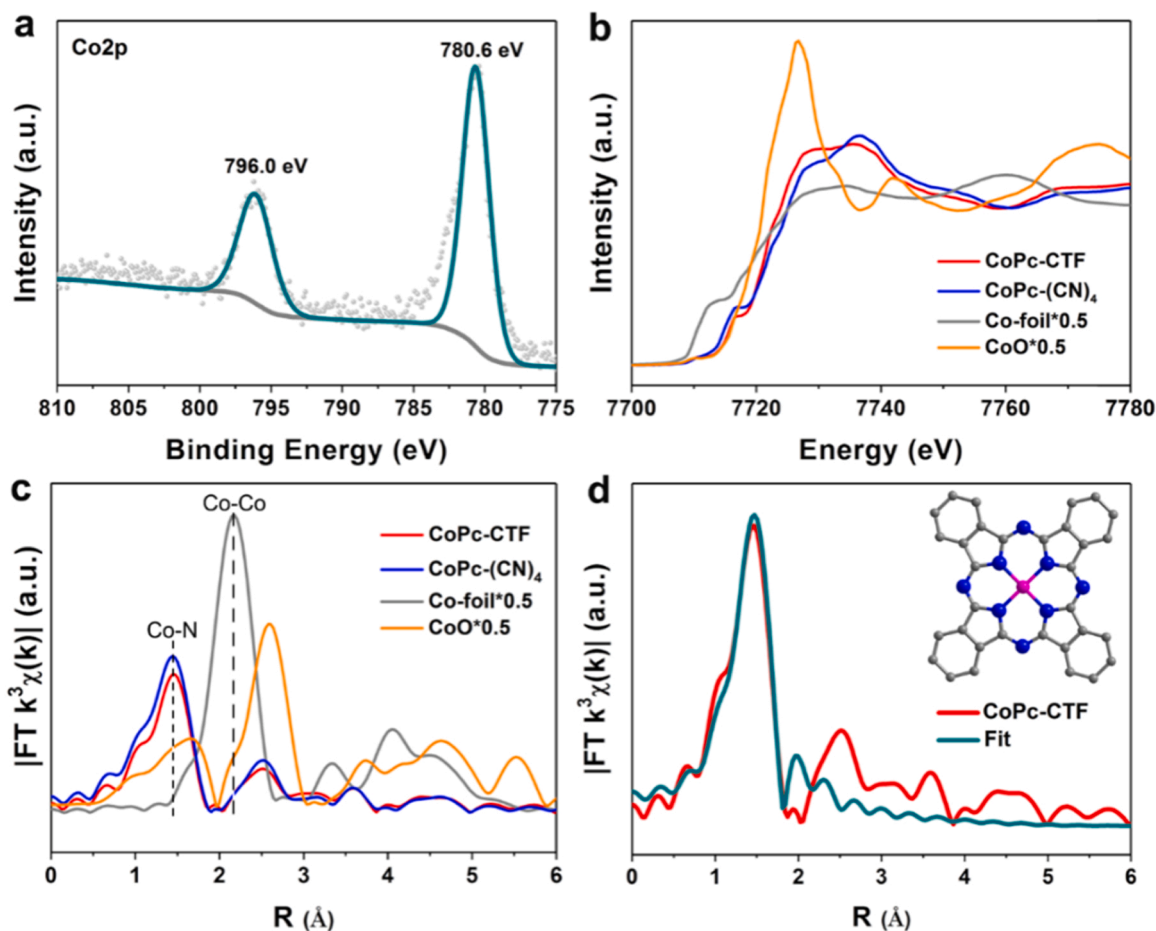

Fig. 2. Structural characterization of CoPc–CTF. (a) XPS spectra of the Co 2p region of CoPc–CTF. (b) Normalized Co K–edge XANES spectra of Co foil, CoPc–(CN)₄, CoPc–CTF, and CoO. (c) Fourier transform EXAFS spectra of different samples. (d) The corresponding EXAFS fitting curves of CoPc–CTF.

targeted structure. The SEM and TEM images of NiPc–CTF indicated that this framework also had cross–linked nanobelts morphology (Fig. S11). The intrinsic N and Ni element were all homogeneously distributed throughout the nanoscale networks in NiPc–CTF. ICP suggested that the Ni content of NiPc–CTF was 3.91 wt% (Table S1). The XPS and XAS analyses on NiPc–CTF revealed that Ni atoms carried positive charges between metallic Ni(0) and the oxidized states Ni(II) and exist most likely as atomically isolated Ni atoms in the form of Ni–N$_4$ structure (Fig. S12–S13 and Table S2).

3.2. Electrocatalytic Performance

3.2.1. The electrocatalytic performances of MPc–CTF in neutral media

To evaluate the catalytic CO$_2$RR performances of the MPc–CTF (M = Co, Ni). Firstly, the performance of MPc–CTF (M = Co, Ni) catalysts was performed in a typical H–cell in neutral media filled with 0.5 M KHCO$_3$ electrolyte (Fig. S14). All the potentials mentioned in this work are with reference to the reversible hydrogen electrode (RHE), and all electrochemical measurements in this work are at room temperature (298 K, 1 bar). The selection of KHCO$_3$ electrolyte is to keep neutral pH and suppress the HER at the same time. As revealed by the linear sweep voltammetry (LSV) curves of MPc–CTF (M = Co, Ni) between 0 and −1.2 V in Fig. 3a, the onset potentials of these catalysts in CO$_2$–saturated 0.5 M KHCO$_3$ aqueous solution (pH = 7.2) are more positive than those in corresponding Ar–saturated electrolyte, manifesting their CO$_2$RR activities. Notably, CoPc–CTF afforded a more positive onset potential (−0.39 versus −0.50 V) and much higher geometric cathodic current density (54.3 versus 36.4 mA cm^{-2} at −1.2 V) than those of NiPc–CTF under the same condition (Fig. 3a), indicating much higher CO$_2$RR activity of CoPc–CTF than that of NiPc–CTF. The difference in reactivity between Co and Ni should depend on the reactivity of the metal itself to bind and activate CO$_2$. A low interfacial charge–transfer resistance (R$_{CT}$, Fig. S15) for CoPc–CTF indicates that it has good conductivity and is in favor of electron transfer to active sites.

To determine the products of the CO$_2$RR by MPc–CTF (M = Co, Ni) catalysts, we quantitatively analyzed the gas and liquid reduction products by gas chromatography (GC) and ^{1}H NMR spectroscopy, respectively. Notably, for CoPc–CTF and NiPc–CTF catalysts, only CO and H$_2$ were detected as the gas products, and no liquid product was produced in the electrolyte solution over the applied potential range of −0.6 to −1.2 V. As shown in Fig. 3b, CO can be reliably detected at −0.6 V, and the FE$_{CO}$ of CoPc–CTF increased to 96.9% at −0.9 V and kept close to 100% in a wide potential window range from −0.8 to −1.1 V. Notably, only H$_2$ was obtained throughout the testing range of −0.8 to −1.2 V when using metal–free phthalocyanine monomer (H$_2$Pc) as catalyst, indicating that the Co–N$_4$ units in CoPc–CTF are the active sites (Fig. S16). The NiPc–CTF showed the maximum FE$_{CO}$ value of 94.9% at −0.9 V, and then quickly dropped along with the increase of. the potentials. Correspondingly, NiPc–CTF exhibited the quick increase of FE$_{H_2}$ with the increase of negative potentials (Fig. S17). Furthermore, the CO partial current densities of CoPc–CTF were linearly increased when a more negative potential was gradually applied, reaching a maximum value of 47.6 mA cm^{-2} at −1.2 V, which was significantly higher than that of NiPc–CTF (the maximum J_{CO} as −8.4 mA cm^{-2} at −0.9 V) (Fig. 3c and Fig. S18–S19). In addition, the turnover frequency (TOF) of the CoPc–CTF gradually increased with the increasing potentials, reaching a maximum value of 13212 h^{-1} at −1.2 V, while the maximum TOF value of NiPc–CTF was only 2448 h^{-1} at −0.9 V (Fig. 3d and Fig. S20). To the best of our knowledge, the CO partial current density of CoPc–CTF (26.6 mA cm^{-2} at −0.9 V and 47.6 mA cm^{-2} at −1.2 V) also outperforms other phthalocyanine–based composites and COFs electrocatalysts in similar reaction systems within H–type electrochemical cell (Fig. 3e and Table S3), such as CuPcF$_8$–CoNPc–COF (14.6 mA cm^{-2} at −0.62 V) [65], CoPc–PDQ–COF (22.2 mA cm^{-2} at −0.66 V) [66], CoPc–PI–COF–1 (21.2 mA cm^{-2} at −0.9 V) [67], NiPc–TFPN COF–light (17.5 mA cm^{-2} at −0.9 V) [68], CoPc–PI–COF–3 (31.7 mA cm^{-2} at −0.9 V) [69], NiPc–COF (35 mA cm^{-2} at −1.1 V) [55]. The superior CO$_2$RR performance of the
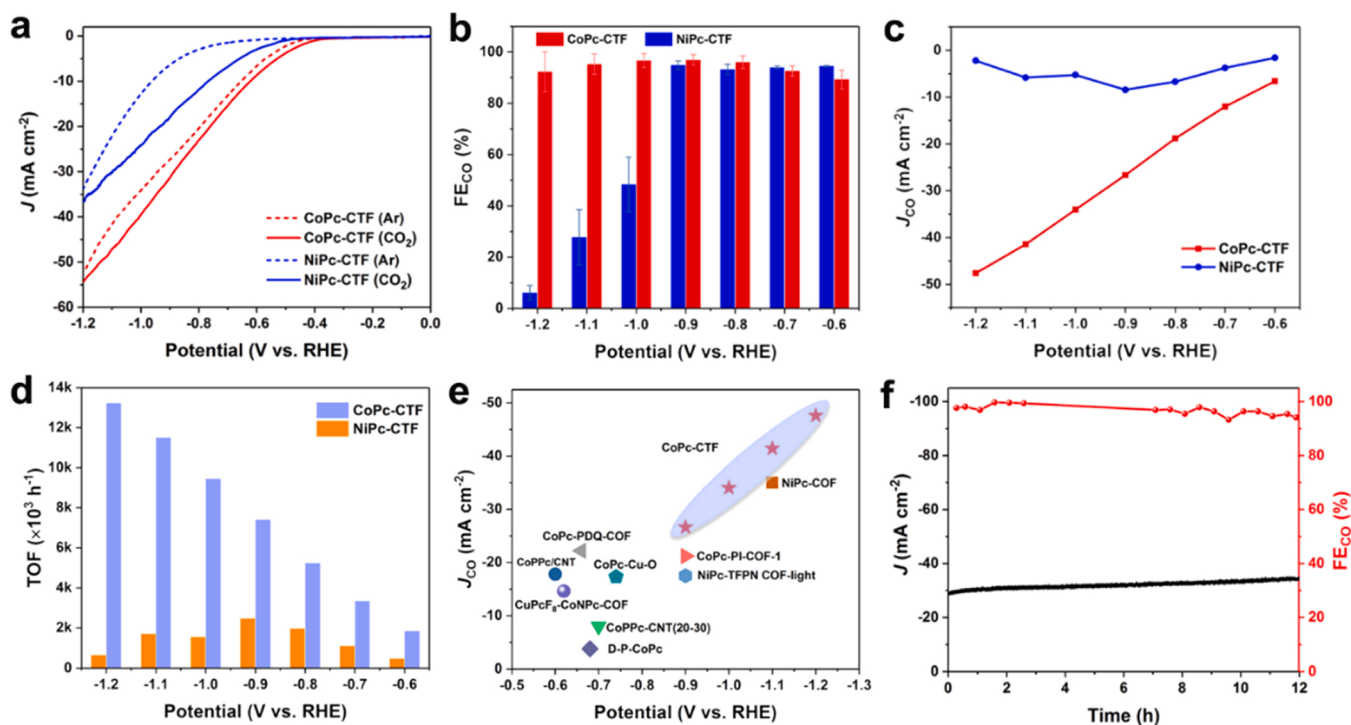

Fig. 3. Electrocatalytic CO$_2$RR performance in neutral media in an H–type cell system. (a) LSV curves in Ar (dot) or CO$_2$–saturated (solid) 0.5 M KHCO$_3$ at 10 mV s^{-1}, (b) Faradaic efficiency of CO, (c) CO partial current densities for CoPc–CTF and NiPc–CTF at different potentials. (d) Turnover frequency of CO by CoPc–CTF and NiPc–CTF. (e) Comparison of J_{CO} values between CoPc–CTF and other reported phthalocyanine–based electrocatalysts evaluated in H–type cells. (f) Long–term stability test of CoPc–CTF at −0.9 V for 12 h.

CoPc–CTF makes it stand out among recently reported phthalocyanine–based catalysts for CO generation in terms of CO partial current density (Table S3). The excellent CO_2RR performance of CoPc–CTF could be attributed to the robust conjugated framework, atomically isolated Co atoms in the form of Co–N_4 structure as well as the functional triazine groups. These results are supported by XAS and XPS analyses after catalysis of CoPc–CTF.

The long–term stability of electrocatalysts should be evaluated for any potential practical applications. As shown in Fig. 3 f, CoPc–CTF can constantly deliver a current density of about −29.3 mA cm⁻² at −0.9 V for 12 h, and keep the high CO selectivity of about 94.3%. Thus, CoPc–CTF shows good stability in this neutral aqueous media with continuous production of CO, as evidenced by the almost unchanged total current density and FE_{CO}. The morphology of CoPc–CTF morphology is well retained after electrocatalysis based on SEM image (Fig. S21). No Co NPs are observed and Co, C, N element are homogeneously distributed throughout in the CoPc–CTF based on TEM images after electrocatalysis (Fig. S22). Moreover, the Co 2p XPS spectra of the CoPc–CTF after electrocatalysis are almost the same as the initial ones

(Fig. S23), and the Co K–edge XANES and EXAFS of CoPc–CTF after electrolysis show that no obvious change occurred (Fig. S24), suggesting that the structure of the CoPc–CTF remains intact and no crystalline metal impurities generated during the CO_2RR process. We also tested CoPc-CTF for its performance in a gas diffusion flow cell with neutral media CO_2-saturated 0.5 M $KHCO_3$ electrolyte. As shown in Fig. S25, CoPc-CTF shows high Faradaic efficiency over 95% in a wide potential window range from −0.7 to −1.1 V. Furthermore, the CO partial current densities of CoPc–CTF reach 165.9 mA cm⁻² at −1.2 V.

3.2.2. The electrocatalytic performances of CoPc–CTF in alkaline media

CoPc–CTF with excellent CO_2RR performance in near–neutral media of 0.5 M $KHCO_3$ (pH = 7.2) encouraged us to integrate the catalyst into the gas diffusion electrodes (GDE) in alkaline media to meet the commercialization requirements (> 200 mA cm⁻²). Generally, flow–cell can permit CO_2 to diffuse rapidly to catalyst surface, and form gas–liquid–solid interfaces resulting in a large increase of local CO_2 concentration, and high local pH is also favorable for suppressing HER (Fig. 4a). Therefore, the CO_2RR performance of CoPc–CTF was further
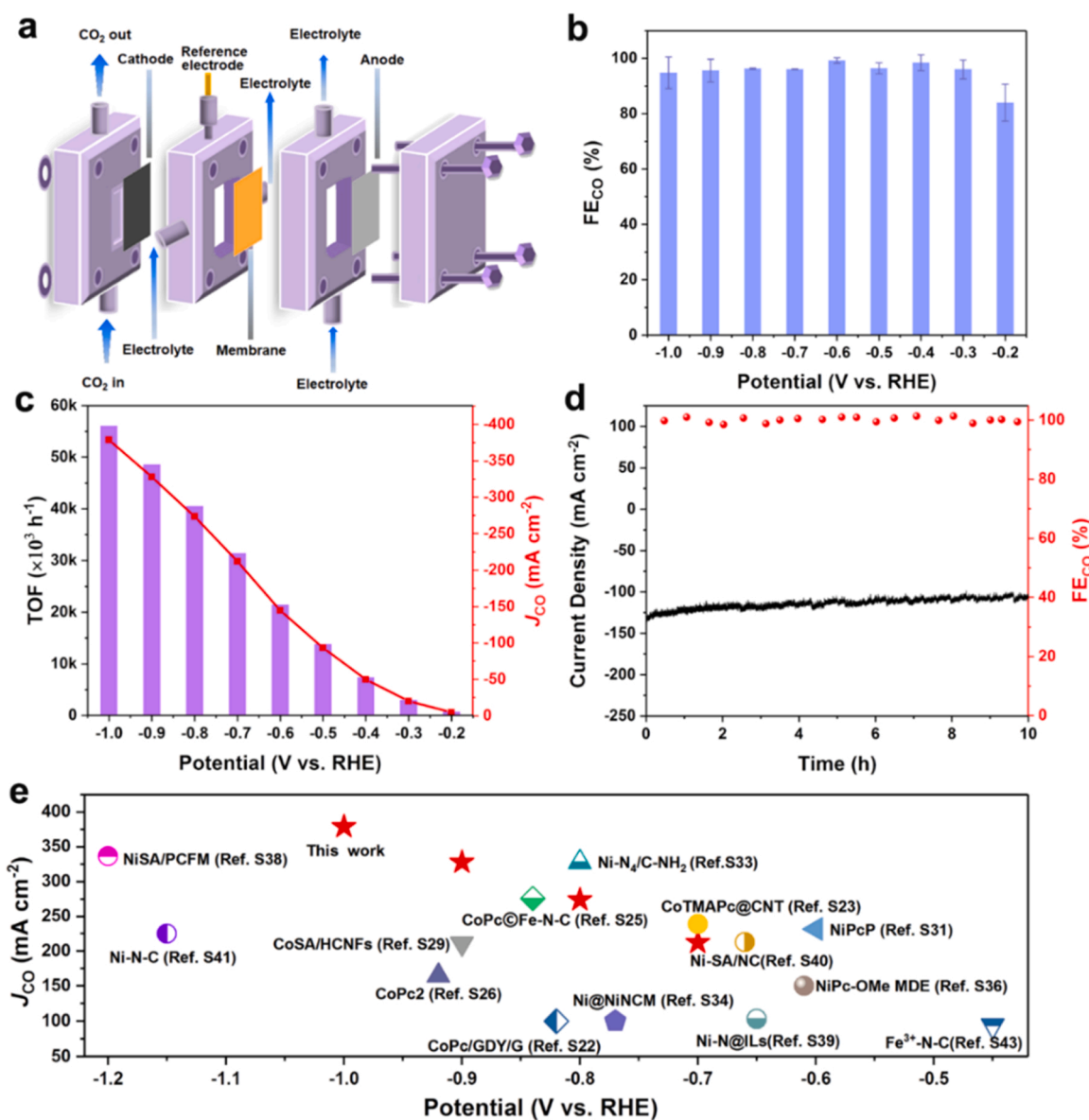

Fig. 4. Electrocatalytic CO_2RR performance in a flow cell system in alkaline media. (a) Schematic of a flow cell configuration. (b) Faradaic efficiency of CO for CoPc–CTF in 1 M KOH. (c) Turnover frequency and CO partial current density for CoPc–CTF. (d) Long–term stability test of CoPc–CTF at −0.6 V. (e) Comparison of J_{CO} for CoPc–CTF and recently reported electrocatalysts for CO_2RR.

investigated in a flow cell with CO_2–saturated 1 M KOH (pH = 13.4) as electrolyte. Interestingly, the high FE_{CO} of CoPc–CTF can reach 99.2% at −0.6 V, and over 94% in a wide applied potential range between −0.3 and −1.0 V (Fig. 4b). Meanwhile, CoPc–CTF achieved an industry level CO partial current density of 378.8 mA cm^{-2} at −1.0 V (Fig. 4c and Fig. S26–S27), which is about 11 times that in an H–type cell (34.0 mA cm^{-2} at −1.0 V). In addition, CoPc–CTF presented a high TOF of 56088 h^{-1} at the applied potential of − 1.0 V (Fig. 4c). No significant attenuation of current density and FE_{CO} were observed after 10 h electrolysis (Fig. 4d), indicating the excellent durability of the CoPc–CTF catalyst in the flow cell configuration. To get insight into the active sites of CoPc-CTF during the process of CO_2RR, we did in-situ Raman spectroscopy (Fig. S28) to demonstrate that the CoN_4 active sites in CoPc-CTF should be stable in CO_2RR process, being consistent with TEM, XPS results (Fig. S29–S30). To the best of our knowledge, such high CO partial current densities of CoPc–CTF surpassed most of reported electrocatalysts (Fig. 4e, Table S4), making CoPc–CTF one of the state-–of–the–art electrocatalysts for the CO_2RR. The high CO partial current density and nearly 100% selectivity for CO production over CoPc–CTF would make it a promising material for further commercial application.

3.2.3. The electrocatalytic performances of CoPc–CTF in acidic media

CO_2 electrolysis in an acidic media offers an alternative strategy to increase CO_2 utilization efficiency, but is quite challenging due to the associated competitive HER [23,24]. Moreover, it is very difficult to develop heterogeneous electrocatalysts in acidic media. Covalent triazine frameworks (CTFs) are known to have remarkable chemical

stabilities. Since our CoPc–CTF was prepared under strong acidic conditions, we then explored the CO_2RR performance in acidic media. The CO_2RR activity of CoPc-CTF was investigated in a flow cell in the phosphoric acidic electrolyte (0.5 M H_3PO_4, 0.5 M KH_2PO_4, and 1.5 M KCl, pH = 2). As shown in Fig. 5a, the FE_{CO} of CoPc–CTF can reach up to 94.3% at −1.2 V, and over 90% in a wide applied potential range between –1.0 and –1.5 V. Meanwhile, the J_{CO} of CoPc–CTF gradually increases with the increase of the overpotential, reaching 172.5 mA cm^{-2} at −1.5 V (Fig. 5a), which outperforms all noble metal–free electrocatalysts for CO_2RR in acidic reaction systems (Fig. 5d and Table S5), and about two times that of CoPc molecule (Fig. 5c and Fig. S31). To estimate the electrochemical active surface area (ECSA) of CoPc-CTF and CoPc molecule, we performed cyclic voltammetry to measure the double-layer capacitance (C_{dl}) (Fig. S32). The results showed that the C_{dl} value of CoPc-CTF (8.47 mF cm^{-2}) is higher than that of CoPc (7.77 mF cm^{-2}). Moreover, CoPc–CTF shows a high 44% half–cell cathodic energy efficiency (EE), which is about two times than that of CoPc molecule with an EE of 26%. CoPc-CTF shows high single pass carbon efficiency (SPCE) up to 51.3% in acidic electrolyte with a CO_2 flow rate of 1.45 sccm (Fig. S33). The results highlight the importance of covalent triazine network towards enhancement CO_2RR in comparison with molecule. The long–term stability is an important factor for evaluating the practicability of catalytic materials. As shown in Fig. 5b, the CoPc–CTF is capable of delivering current densities of 150.0 mA cm^{-2}, after 10 h catalysis durability test. The high CO selectivity over 93.2% for CoPc–CTF was still maintained (Fig. 5b). Moreover, no Co NPs were observed in the TEM images of the CoPc–CTF after electrocatalysis in
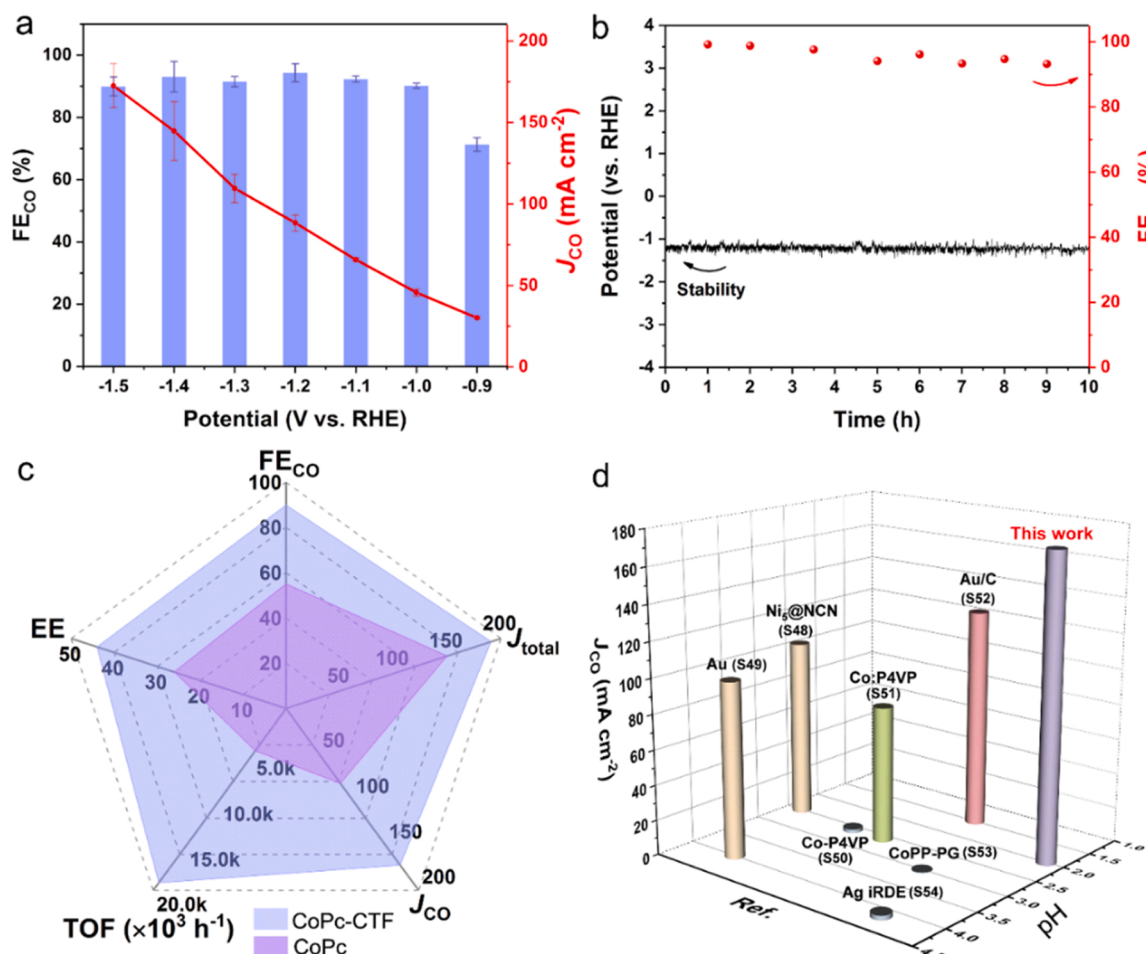

Fig. 5. Electrocatalytic CO_2RR performance in a flow cell in acidic media. (a) FE_{CO} and Jco for CoPc–CTF in the phosphoric acidic electrolyte (0.5 M H_3PO_4, 0.5 M KH_2PO_4, and 1.5 M KCl, pH = 2). (b) Long–term stability test of CoPc–CTF at −150.0 mA cm^{-2}. (c) Comparison of performance parameters at −1.5 V of CoPc–CTF and CoPc. (d) Comparison of pH and Jco for CoPc–CTF and recently reported catalysts in acidic media (Ref. is reference).

acidic media (Fig. S34), suggesting that no crystalline metal impurities generated during the CO_2RR process. Furthermore, the peak of Co–N at 1.44 Å is remained in the EXAFS of CoPc–CTF after the CO_2RR measurement (CoPc–CTF–tested) and the EXAFS fitting average coordination number of Co–N is 4.0 (Fig. S35), indicating that the Co–N_4 structure of CoPc–CTF remained intact in the acidic testing system. The excellent CO_2RR performance in acidic media indicates that the use of CoPc–CTF might contribute to more efficient CO_2 utilization and energy savings in potential industrial applications.

3.3. The DFT calculation and reaction mechanism

In order to investigate the source of CO in the CO_2RR process, the $^{13}CO_2$–reduction isotope experiments were performed at −0.9 V in H-cell, and the gas products were analyzed by gas chromatography–mass spectrometry (GC–MS). As shown in Fig. S36, when $^{12}CO_2$ was replaced by $^{13}CO_2$ in 0.5 M $KH^{12}CO_3$ electrolyte, both the signals of ^{12}CO ($m/z = 28$) and ^{13}CO ($m/z = 29$) were observed, while only ^{13}CO was produced by using 0.5 M KCl as electrolyte (Fig. S36b). The results suggested that CO was stemmed from CO_2 in equilibrium with HCO_3^- in CO_2–saturated $KHCO_3$ solution [70–72].

Operando attenuated total reflectance Fourier transform infrared spectroscopy (ATR–FTIR) modes were collected to identify possible reaction intermediates over CoPc–CTF and gain insight into the underlying CO_2RR mechanism. As shown in Fig. S38 the downward peak at 1398 cm^{-1} appeared and can be ascribed to intermediate of *COOH, which is recognized as the key intermediate for the formation of CO [73]. Meanwhile, the integrated *COOH signal gradually increased with the reaction time and then reached dynamic balanced, suggesting that the formation intermediate of *COOH was the rate determining step reaction for CoPc–CTF.

To further investigate the catalytic mechanism on CoPc–CTF, we performed density functional theory (DFT) calculations for the energies of the CO_2RR and HER process, using the triazine functionalized Co–N_4 structure to simulate the experimental CoPc–CTF structure (Fig. S39–S40). In general, the CO production by CO_2RR is a two proton–coupled electron transfer (PCET) process (Fig. 6a). Firstly, the CO_2 molecule is absorbed on the Co–N_4 site and forms the *COOH intermediate by a PCET. Subsequently, the *COOH is converted to *CO via releasing one H_2O molecule, and finally the *CO is desorbed from the Co–N_4 to afford the targeted CO product. For CoPc–CTF, we found that the formation of *COOH is the rate–determining step (RDS) of CO_2RR and the energy on Co site is 1.84 eV (Fig. 6b), which is lower than that of the formation *H (1.90 eV) in HER process (Fig. S41–S42). The result indicated that the CO generation would be promoted rather than the competitive side reaction of HER. In contrast, the corresponding energy for CO_2RR (2.24 eV, Fig. 6b) by CoPc molecule is higher than that of HER (2.08 eV, Fig. S43), which indicates that HER takes precedence on CoPc molecule. Moreover, the energy for RDS on the CoPc–CTF (1.84 eV) is significantly lower than that on CoPc molecule (2.24 eV),
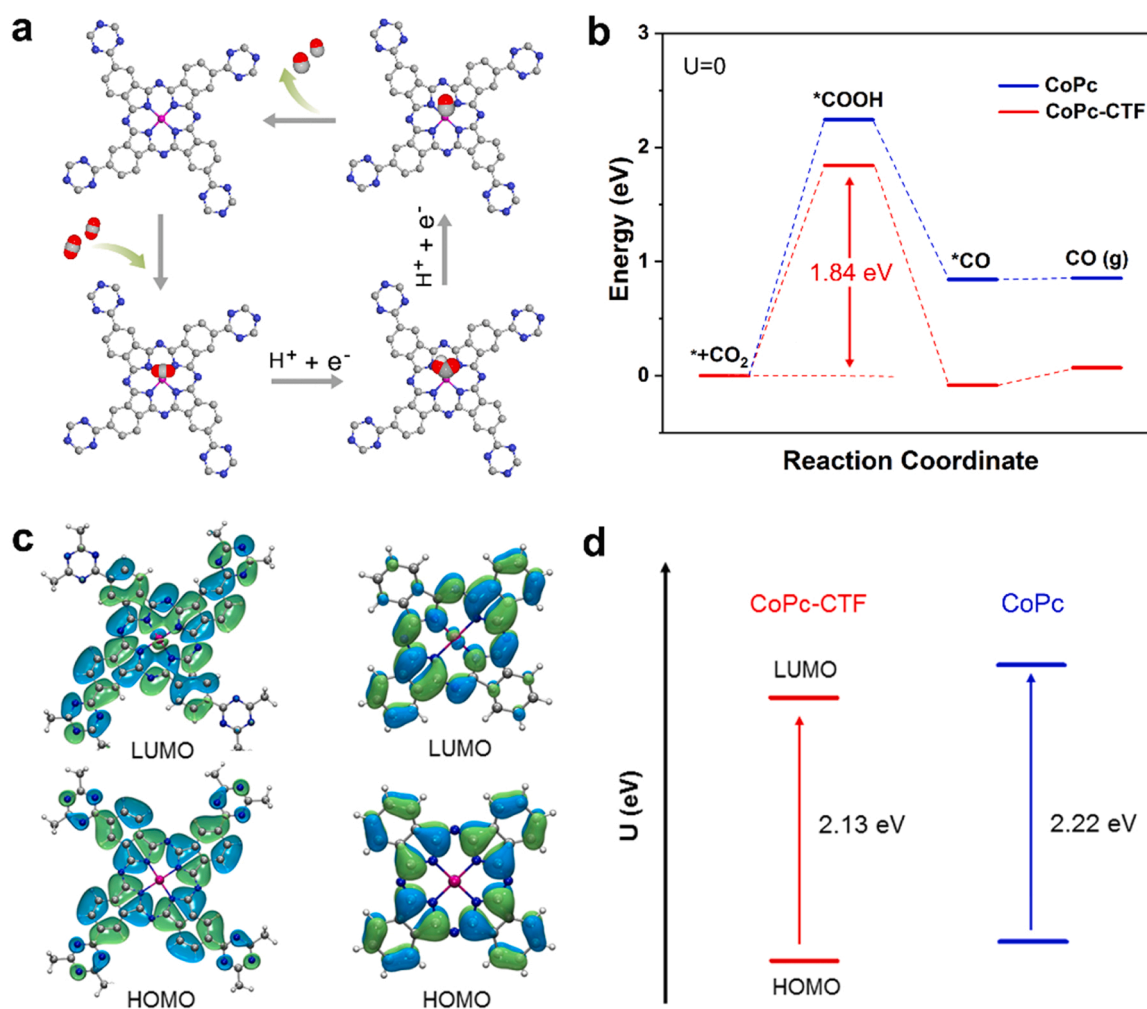

Fig. 6. Density functional theory calculations and proposed schematic mechanism of CoPc–CTF. (a) A proposed catalytic mechanism of CoPc–CTF for CO_2RR. Co: pink; N: blue; C: gray; O: red; H: white. (b) Energy diagrams CO_2RR of CoPc–CTF and CoPc. (c) The charge distributions of CoPc–CTF (Left) and CoPc (Right) and (d) The HOMO–LUMO gap of CoPc–CTF and CoPc.

which indicates that CoPc–CTF with covalent triazine network is in favor of CO_2RR. The above DFT calculated results are in accordance with the experiment results that CoPc–CTF showed higher CO Faradaic efficiency and CO partial current density than those of CoPc molecule (Fig. 5c and Fig. S31). The excellent CO_2RR performances of CoPc–CTF can be further explained in terms of HOMO–LUMO gap. The HOMO–LUMO gap (2.13 eV) of CoPc–CTF is smaller than that of CoPc molecule (2.22 eV), which is beneficial to electron transfer and enhanced conductivity (Figs. 6c–6d) [74]. The increased conductivity of CoPc–CTF was evidenced by a reduced resistivity found in electrochemical impedance spectroscopy (Fig. S15). Moreover, the FE_{CO} values of CoPc–CTF are higher than monomer CoPc–$(CN)_4$ (Fig. S44–S46) in near–neutral, alkaline and acidic media, indicating that the functional triazine polymer of CoPc–CTF could promote the CO_2 reduction to product CO. The results indicated that the catalytic capability of the Co active site has been significantly improved when the phthalocyanine molecules are integrated into the covalent triazine network to form CoPc–CTF.

4. Conclusion

In conclusion, we have exploited a facile pyrolysis–free method to achieve robust conjugated metallophthalocyanine–based covalent triazine frameworks MPc–CTF for efficient CO_2RR with high current density and high Faradaic efficiency in a full pH range, namely near–neutral media, alkaline media, or acidic media. The optimal CoPc–CTF electrocatalyst shows close to 100% CO selectivity and a high J_{CO} of 47.6 mA cm^{-2} at -1.2 V in neutral media (pH = 7.2). Importantly, CoPc–CTF has achieved a high TOF of 56088 h^{-1} and a very large J_{CO} of 378.8 mA cm^{-2} at -1.0 V in alkaline media (pH = 13.4). Particularly, CoPc–CTF could show maximum a FE_{CO} of 94.3% and J_{CO} of 172.5 mA cm^{-2} in acidic electrolyte (pH = 2). Experimental characterizations reveal the importance of chemically conjugated framework, atomically isolated Co atoms in the form of Co–N_4 structure as well as the functional triazine groups for enhanced CO_2RR performance on CoPc–CTF. DFT calculations suggest that the CO_2 reduction to produce CO process would be more favorable than HER in CoPC–CTF. Moreover, further studies indicate that the functional triazine moiety of CoPc–CTF probably lowered the energy (1.84 eV) for *COOH than that (2.24 eV) of the CoPc molecule, and that CoPc–CTF has smaller HOMO–LUMO gap than that of CoPc. It can be seen more conjugated triazine–based framework materials will be rationally designed and prepared via this facile approach for energy and catalysis applications in the future.

CRediT authorship contribution statement

Qiao Wu: Conceptualization, Investigation, Writing – original draft. **Duan-Hui Si**: DFT calculation. **Jun Liang**: Validation, Software. **Yuan-Biao Huang**: Conceptualization, Writing – review & editing. **Rong Cao**: Conceptualization, Supervision, Funding acquisition.

Declaration of Competing Interest

The authors declare that they have no known competing financial interests or personal relationships that could have appeared to influence the work reported in this paper.

Data Availability

Data will be made available on request.

Appendix A. Supporting information

Supplementary data associated with this article can be found in the online version at doi:10.1016/j.apcatb.2023.122803.

References

[1] M. Liu, Y. Pang, B. Zhang, P. De Luna, O. Voznyy, J. Xu, X. Zheng, C.T. Dinh, F. Fan, C. Cao, F.P. de Arquer, T.S. Safaei, A. Mepham, A. Klinkova, E. Kumacheva, T. Filleter, D. Sinton, S.O. Kelley, E.H. Sargent, Enhanced electrocatalytic CO_2 reduction via field–induced reagent concentration, Nature 537 (2016) 382–386.

[2] H. Fei, J. Dong, Y. Feng, C.S. Allen, C. Wan, B. Volosskiy, M. Li, Z. Zhao, Y. Wang, H. Sun, P. An, W. Chen, Z. Guo, C. Lee, D. Chen, I. Shakir, M. Liu, T. Hu, Y. Li, A. I. Kirkland, X. Duan, Y. Huang, General synthesis and definitive structural identification of MN_4C_4 single-atom catalysts with tunable electrocatalytic activities, Nat. Catal. 1 (2018) 63–72.

[3] J. Liang, Q. Wu, Y.B. Huang, R. Cao, Reticular frameworks and their derived materials for CO_2 conversion by thermo−catalysis, EnergyChem 3 (2021), 100064.

[4] C.L. Rooney, Y. Wu, Z. Tao, H. Wang, Electrochemical reductive n-methylation with CO_2 enabled by a molecular catalyst, J. Am. Chem. Soc. 143 (2021) 19983–19991.

[5] F.P. Pan, W. Deng, C. Justiniano, Y. Li, Identification of champion transition metals centers in metal and nitrogencodoped carbon catalysts for CO_2 reduction, Appl. Catal. B Environ. 226 (2018) 463–472.

[6] J.D. Yi, D.H. Si, R. Xie, Q. Yin, M.D. Zhang, Q. Wu, G.L. Chai, Y.B. Huang, R. Cao, Conductive two–dimensional phthalocyanine–based metal–organic framework nanosheets for efficient electroreduction of CO_2, Angew. Chem. Int. Ed. 60 (2021) 17108–17114.

[7] Q. Wu, R.–K. Xie, M.–J. Mao, G.–L. Chai, J.–D. Yi, S.–S. Zhao, Y.–B. Huang, R. Cao, Integration of strong electron transporter tetrathiafulvalene into metalloporphyrin–based covalent organic framework for highly efficient electroreduction of CO_2, ACS Energy Lett. 5 (2020) 1005–1012.

[8] H.P. Yang, Q. Lin, C. Zhang, X.Y. Yu, Z. Cheng, G.D. Li, Q. Hu, X.Z. Ren, Q.L. Zhang, J.H. Liu, C.X. He, Carbon dioxide electroreduction on single-atom nickel decorated carbon membranes with industry compatible current densities, Nat. Commun. 11 (2020) 593.

[9] T.T. Zheng, K. Jiang, N. Ta, Y.F. Hu, J. Zeng, J.Y. Liu, H.T. Wang, Large-scale and highly selective CO_2 electrocatalytic reduction on nickel single-atom catalyst, Joule 3 (2019) 265–278.

[10] Q.J. Wu, D.H. Si, Q. Wu, Y.L. Dong, R. Cao, Y.B. Huang, Boosting electroreduction of CO_2 over cationic covalent organic frameworks: hydrogen bonding effects of halogen ions, Angew. Chem. Int. Ed. 62 (2023) e202215687.

[11] D.D. Ma, S.G. Han, C.S. Cao, X.F. Li, X.T. Wu, Q.L. Zhu, Remarkable electrocatalytic CO_2 reduction with ultrahigh CO/H_2 ratio over single-molecularly immobilized pyrrolidinonyl nickel phthalocyanine, Appl. Catal. B Environ. 264 (2020), 118530.

[12] M. Zhao, Y. Gu, W. Gao, P. Cui, H. Tang, X. Wei, H. Zhu, G. Li, S. Yan, X. Zhang, Z. Zou, Atom vacancies induced electron-rich surface of ultrathin Bi nanosheet for efficient electrochemical CO_2 reduction, Appl. Catal. B Environ. 266 (2020), 118625.

[13] M.N. Zhu, B.W. Zhang, M.R. Gao, P.F. Sui, C.Y. Xu, L. Gong, H.B. Zeng, K. Shankar, S. Bergens, J.L. Luo, Electrochemically reconstructed perovskite with cooperative catalytic sites for CO_2-to-formate conversion, Appl. Catal. B Environ. 306 (2022), 121101.

[14] C. Zhao, Y. Wang, Z. Li, W. Chen, Q. Xu, D. He, D. Xi, Q. Zhang, T. Yuan, Y. Qu, J. Yang, F. Zhou, Z. Yang, X. Wang, J. Wang, J. Luo, Y. Li, H. Duan, Y. Wu, Y. Li, Solid–diffusion synthesis of single–atom catalysts directly from bulk metal for efficient CO_2 reduction, Joule 3 (2019) 584–594.

[15] W.F. Xiong, D.H. Si, J. D, Y, Y.B. Huang, H.F. Li, R. Cao, Morphology and composition dependence of multicomponent Cu-based nanoreactor for tandem electrocatalysis CO_2 reduction, Appl. Catal. B Environ. 314 (2022), 121498.

[16] L. Zeng, J.W. Chen, L.X. Zhong, W.W. Zhen, Y.Y. Tay, S.Z. Li, Y.G. Wang, L. M. Huang, C. Xue, Synergistic effect of Ru-N_4 sites and Cu-N_3 sites in carbon nitride for highly selective photocatalytic reduction of CO_2 to methane, Appl. Catal. B Environ. 307 (2022), 121154.

[17] H. Yang, Y. Wu, G. Li, Q. Lin, Q. Hu, Q. Zhang, J. Liu, C. He, Scalable production of efficient single–atom copper decorated carbon membranes for CO_2 electroreduction to methanol, J. Am. Chem. Soc. 41 (2019) 12717–12723.

[18] Y.S. Wu, Z. Jiang, X. Lu, Y.Y. Liang, H.L. Wang, Domino electroreduction of CO_2 to methanol on a molecular catalyst, Nature 575 (2019) 639.

[19] X.Q. Li, G.Y. Duan, J.W. Chen, L.J. Han, S.J. Zhang, B.H. Xu, Regulating electrochemical CO_2RR selectivity at industrial current densities by structuring copper@poly(ionic liquid) interface, Appl. Catal. B Environ. 297 (2021), 120471.

[20] Y. Pan, H.D. Li, J. Xiong, Y., D. Yu, H.Y. Du, S.X. Li, Z.C. Wu, S.P. Li, J.P. Lai, L. Wang, Protecting the state of Cu clusters and nanoconfinement engineering over hollow mesoporous carbon spheres for electrocatalytical C-C coupling, Appl. Catal. B Environ. 306 (2022), 121111.

[21] T.H.M. Pham, J. Zhang, M. Li, T.–H. Shen, Y. Ko, V. Tileli, W. Luo, A. Züttel, Enhanced electrocatalytic CO_2 reduction to C2+ products by adjusting the local reaction environment with polymer binders, Adv. Energy Mater. 12 (2022), 2103663.

[22] C. Chen, X. Yan, S. Liu, Y. Wu, Q. Wan, X. Sun, Q. Zhu, H. Liu, J. Ma, L. Zheng, H. Wu, B. Han, Highly efficient electroreduction of CO_2 to C2+ alcohols on heterogeneous dual active sites, Angew. Chem. Int. Ed. 59 (2020) 16459–16464.

[23] J. Huang, F. Ozden, A. Rasouli, F. Arquer, S. Liu, S. Zhang, M. Luo, X. Wang, Y. Lum, Y. Xu, K. Bertens, R.K. Miao, C. Dinh, D. Sinton, E.H. Sargent, CO_2 electrolysis to multicarbon products in strong acid, Science 372 (2021) 1074–1078.

[24] J. Gu, S. Liu, W.Y. Ni, W.H. Ren, S. Haussener, X.L. Hu, Modulating electric field distribution by alkali cations for CO_2 electroreduction in strongly acidic medium, Nat. Catal. 5 (2022) 268–276.

[25] S. Ringe, C.G. Morales–Guio, L.D. Chen, M. Fields, T.F. Jaramillo, C. Hahn, K. Chan, Double layer charging driven carbon dioxide adsorption limits the rate of electrochemical carbon dioxide reduction on Gold, Nat. Commun. 11 (2020) 33.

[26] N. Sikdar, J. Junqueira, S. Dieckhofer, T. Quast, M. Braun, Y. Song, H. Aiyappa, S. Seisel, J. Weidner, D. Ohl, C. Andronescu, W. Schuhmann, A metal–organic framework derived $Cu_xO_yC_z$ catalyst for electrochemical CO_2 reduction and impact of local pH change, Angew. Chem. Int. Ed. 60 (2021) 23427–23434.

[27] A.S. Varela, M. Kroschel, T. Reier, P. Strasser, Controlling the selectivity of CO_2 electroreduction on copper: the effect of the electrolyte concentration and the importance of the local pH, Catal. Today 260 (2016) 8–13.

[28] F.P.G. d Arquer, C.–T. Dinh, A. Ozden, J. Wicks, C. McCallum, A.R. Kirmani, D.–H. Nam, C. Gabardo, A. Seifitokaldani, X. Wang, Y.C. Li, F. Li, J. Edwards, L. J. Richter, S.J. Thorpe, D. Sinton, E.H. Sargent, CO_2 electrolysis to multicarbon products at activities greater than 1 A cm^{-2}, Science 367 (2020) 661–666.

[29] C. Kim, J.C. Bui, X. Luo, J.K. Cooper, A. Kusoglu, A.Z. Weber, A.T. Bell, Tailored catalyst microenvironments for CO_2 electroreduction to multicarbon products on copper using bilayer ionomer coatings, Nat. Energy 6 (2021) 1026–1034.

[30] Y. Wang, H. Shen, K.J.T. Livi, D. Raciti, H. Zong, J. Gregg, M. Onadeko, Y. Wan, A. Watson, C. Wang, Copper nanocubes for CO_2 reduction in gas diffusion electrodes, Nano Lett. 19 (2019) 8461–8468.

[31] S. Ren, D. Joulié, D. Salvatore, K. Torbensen, M. Wang, M. Robert, C. P. Berlinguette, Molecular electrocatalysts can mediate fast, selective CO_2 reduction in a flow cell, Science 365 (2019) 367–369.

[32] C. –T. Dinh, F.P. García de Arquer, D. Sinton, E.H. Sargent, High rate, selective, and electroreduction of CO_2 to CO in basic and neutral media, ACS Energy Lett. 3 (2018) 2835–2840.

[33] S. Verma, Y. Hamasaki, C. Kim, W.X. Huang, S. Lu, H.R.M. Jhong, A.A. Gewirth, T. Fujigaya, N. Nakashima, P.J.A. Kenis, Insights into the low Overpotential electroreduction of CO_2 to CO on a supported gold catalyst in an alkaline flow electrolyzer, ACS Energy Lett. 3 (2018) 193–198.

[34] J.A. Rabinowitz, M.W. Kanan, The future of low-temperature carbon dioxide electrolysis depends on solving one basic problem, Nat. Commun. 11 (2020) 5231.

[35] Z. Jiang, Z. Zhang, H. Li, Y. Tang, Y. Yuan, J. Zao, H. Zheng, Y. Liang, Molecular catalyst with near 100% selectivity for CO_2 reduction in acidic electrolytes, Adv. Energy Mater. (2022), 2203603.

[36] W. Deng, L. Zhang, H. Dong, X. Chang, T. Wang, J. Gong, Achieving convenient CO_2 electroreduction and photovoltage in tandem using potential–insensitive disordered Ag nanoparticles, Chem. Sci. 9 (2018) 6599–6604.

[37] T.W. Jiang, Y.W. Zhou, X.Y. Ma, X. Qin, H. Li, C. Ding, B. Jiang, K. Jiang, W.B. Cai, Spectrometric study of electrochemical CO_2 reduction on Pd and Pd–B electrodes, ACS Catal. 11 (2021) 840–848.

[38] J. Gu, C.–S. Hsu, L. c. Bai, H.M. Chen, X.L. Hu, Atomically dispersed Fe^{3+} sites catalyze efficient CO_2 electroreduction to CO, Science 364 (2019) 1091–1094.

[39] Y. Hou, Y.–B. Huang, Y.–L. Liang, G.–L. Chai, J.–D. Yi, T. Zhang, K.–T. Zang, J. Luo, R. Xu, H. Lin, S.–Y. Zhang, H.–M. Wang, R. Cao, Unraveling the reactivity and selectivity of atomically isolated metal–nitrogen sites anchored on porphyrinic triazine frameworks for electroreduction of CO_2, CCS Chem. 1 (2019) 384–395.

[40] H.B. Yang, S.–F. Hung, S. Liu, K. Yuan, S. Miao, L. Zhang, X. Huang, H.–Y. Wang, W. Cai, R. Chen, J. Gao, X. Yang, W. Chen, Y. Huang, H.M. Chen, C.M. Li, T. Zhang, B. Liu, Atomically dispersed Ni(i) as the active site for electrochemical CO_2 reduction, Nat. Energy 3 (2018) 140–147.

[41] C. Yan, H. Li, Y. Ye, H. Wu, F. Cai, R. Si, J. Xiao, S. Miao, S. Xie, F. Yang, Y. Li, G. Wang, X. Bao, Coordinatively unsaturated nickel–nitrogen sites towards selective and high–rate CO_2 electroreduction, Energy Environ. Sci. 11 (2018) 1204–1210.

[42] Y. Hou, J. Liang, Z.–L. Xie, Y.–B. Huang, R. Cao, Spatial sites separation strategy to fabricate atomically isolated nickel catalysts for efficient CO_2 electroreduction, ACS Mater. Lett. 3 (2021) 454–461.

[43] L. Jiao, W. Yang, G. Wan, R. Zhang, X. Zheng, H. Zhou, S.H. Yu, H.L. Jiang, Single–atom electrocatalysts from multivariate MOFs for highly selective reduction of CO_2 at low pressures, Angew. Chem. Int. Ed. 59 (2020) 20589–20595.

[44] S. Ji, Y. Chen, X. Wang, Z. Zhang, D. Wang, Y. Li, Chemical synthesis of single atomic site catalysts, Chem. Rev. 120 (2020) 11900–11955.

[45] X. Liang, N. Fu, S. Yao, Z. Li, Y. Li, The progress and outlook of metal single-atom-site catalysis, J. Am. Chem. Soc. 144 (2022) 18155–18174.

[46] P. Kuhn, M. Antonietti, A. Thomas, A. Porous, Covalent triazine–based frameworks prepared by ionothermal synthesis, Angew. Chem. Int. Ed. 47 (2008) 3450–3453.

[47] P. Kuhn, A. Forget, D.S. Su, A. Thomas, M. Antonietti, From microporous regular frameworks to mesoporous materials with ultrahigh surface area: dynamic reorganization of porous polymer networks, J. Am. Chem. Soc. 130 (2008) 13333–13337.

[48] S. Ren, M.J. Bojdys, R. Dawson, A. Laybourn, Y.Z. Khimyak, D.J. Adams, A. I. Cooper, Porous, fluorescent, covalent triazine–based frameworks via room–temperature and microwave–assisted synthesis, Adv. Mater. 24 (2012) 2357–2361.

[49] R. Xu, D.H. Si, S.S. Zhao, Q.J. Wu, X.S. Wang, T.F. Liu, H. Zhao, R. Cao, Y.B. Huang, Tandem photocatalysis of CO_2 to C_2H_4 via a synergistic rhenium-(i) bipyridine/copper-porphyrinic triazine framework, J. Am. Chem. Soc. 145 (2023) 8261–8270.

[50] Y.S. Li, W.B. Chen, G.L. Xing, D.L. Jiang, L. Chen, New synthetic strategies toward covalent organic frameworks, Chem. Soc. Rev. 49 (2020) 2852–2868.

[51] Y. Yusran, Q.R. Fang, V. Valtchev, Electroactive covalent organic frameworks: design, synthesis, and applications, Adv. Mater. 32 (2020) 2002038.

[52] S. Liu, H.B. Yang, S.F. Hung, J. Ding, W. Cai, L. Liu, J. Gao, X. Li, X. Ren, Z. Kuang, Y. Huang, T. Zhang, B. Liu, Electrifying Model Single–Atom Catalyst for Elucidating the CO_2 Reduction Reaction, Angew. Chem. Int. Ed. 59 (2020) 798–803.

[53] N. Han, Y. Wang, L. Ma, J. Wen, J. Li, H. Zheng, K. Nie, X. Wang, F. Zhao, Y. Li, J. Fan, Z. Zhong, T. Wu, D.J. Miller, J. Lu, S.–T. Lee, Y. Li, Supported cobalt polyphthalocyanine for high–performance electrocatalytic CO_2 reduction, Chem 3 (2017) 652–664.

[54] K.J. Klunder, C.M. Elliott, C.S. Henry, Highly transparent tetraaminophthalocyanine polymer films for DSSC cathodes, J. Mater. Chem. A 6 (2018) 2767–2774.

[55] M.D. Zhang, D.H. Si, J.D. Yi, S.S. Zhao, Y.B. Huang, R. Cao, Conductive phthalocyanine–based covalent organic framework for highly efficient electroreduction of carbon dioxide, Small 16 (2020), 2005254.

[56] X. Suo, F.T. Zhang, Z.Z. Yang, H. Chen, T. Wang, Z.Y. Wang, T. Kobayashi, C.L. Do-Thanh, D. Maltsev, Z.M. Liu, S. Dai, Highly perfluorinated covalent triazine frameworks derived from a low–temperature ionothermal approach towards enhanced CO_2 electroreduction, Angew. Chem. Int. Ed. 60 (2021) 25688–25694.

[57] S. Wei, H. Zou, W. Rong, F. Zhang, Y. Ji, L. Duan, Conjugated nickel phthalocyanine polymer selectively catalyzes CO_2–to–CO conversion in a wide operating potential window, Appl. Catal. B Environ. 284 (2021), 119739.

[58] X. Zhu, C. Tian, S.M. Mahurin, S.H. Chai, C. Wang, S. Brown, G.M. Veith, H. Luo, H. Liu, S. Dai, A. Superacid–Catalyzed, Synthesis of porous membranes based on triazine frameworks for CO_2 separation, J. Am. Chem. Soc. 134 (2012) 10478–10484.

[59] Z. Yang, H. Chen, S. Wang, W. Guo, T. Wang, X. Suo, D.E. Jiang, X. Zhu, I. Popovs, S. Dai, Transformation strategy for highly crystalline covalent triazine frameworks: from staggered AB to eclipsed AA stacking, J. Am. Chem. Soc. 142 (2020) 6856–6860.

[60] M. Szybowicz, W. Bała, K. Fabisiak, K. Paprocki, M. Drozdowski, Micro–Raman spectroscopic investigations of cobalt phthalocyanine thin films deposited on quartz and diamond substrates, Cryst. Res. Technol. 45 (2010) 1265–1271.

[61] T.Y. Gao, Z. Yan, V. Ordomsky, S. Paul, Design of two–dimensional heteropolyacid–covalent organic frameworks composite materials for acid catalysis, ChemCatChem (2022), e202101450.

[62] Y. Cheng, Y. Dong, J. Wu, X. Yang, H. Bai, H. Zheng, D. Ren, Y. Zou, M. Li, Screening melamine adulterant in milk powder with laser Raman spectrometry, J. Food Compos. Anal. 23 (2010) 199–202.

[63] H. Zhang, J. Wei, J. Dong, G. Liu, L. Shi, P. An, G. Zhao, J. Kong, X. Wang, X. Meng, J. Zhang, J. Ye, Efficient visible–light–driven carbon dioxide reduction by a single–atom implanted metal–organic framework, Angew. Chem. Int. Ed. 55 (2016) 14310–14314.

[64] N. Li, W. Lu, K. Pei, W. Chen, Interfacial peroxidase–like catalytic activity of surface–immobilized cobalt phthalocyanine on multiwall carbon nanotubes, RSC Adv. 5 (2015) 9374–9380.

[65] Y. Yue, P. Cai, K. Xu, H. Li, H. Chen, H.C. Zhou, N. Huang, Bimetallic polyphthalocyanine covalent organic frameworks as superior electrocatalystsH, J. Am. Chem. Soc. 143 (2021) 18052–18060.

[66] N. Huang, K.H. Lee, Y. Yue, X. y Xu, S. Irle, Q.H. Jiang, D.L. Jiang, A conductive metallophthalocyanine framework for electrocatalytic carbon dioxide reduction in water, Angew. Chem. Int. Ed. 59 (2020) 16587–16593.

[67] B. Han, X. Ding, B.Q. Yu, H. Wu, W. Zhou, W.P. Liu, C.Y. Wei, B.T. Chen, D.D. Qi, H.L. Wang, K. Wang, Y.L. Chen, B.L. Chen, J.Z. Jiang, Two–dimensional covalent organic frameworks with cobalt(II)phthalocyanine sites for efficient electrocatalytic carbon dioxide reduction, J. Am. Chem. Soc. 143 (2021) 7104–7113.

[68] M. Lu, M. Zhang, C.G. Liu, J. Liu, L.J. Shang, M. Wang, J.N. Chang, S.L. Li, Y. Q. Lan, Dioxin–linked metallophthalocyanine covalent organic frameworks as photo–coupled electrocatalysts for CO_2 reduction, Angew. Chem. Int. Ed. 60 (2021) 4864–4871.

[69] B. Han, Y.H. Jin, B.T. Chen, W. Zhou, B.Q. Yu, C.Y. Wei, H.L. Wang, K. Wang, Y. L. Chen, B.L. Chen, J.Z. Jiang, Maximizing electroactive sites in a three–dimensional covalent organic framework for significantly improved carbon dioxide reduction electrocatalysis, Angew. Chem. Int. Ed. 61 (2022), e202114244.

[70] S. Zhu, B. Jiang, W.B. Cai, M. Shao, Direct observation on reaction intermediates and the role of bicarbonate anions in CO_2 electrochemical reduction reaction on Cu surfaces, J. Am. Chem. Soc. 139 (2017) 15664–15667.

[71] M. Dunwell, Q. Lu, J.M. Heyes, J. Rosen, J.G. Chen, Y.S. Yan, F. Jiao, B.J. Xu, The central role of bicarbonate in the electrochemical reduction of carbon dioxide on gold, J. Am. Chem. Soc. 139 (2017) 3774–3783.

[72] G.B. Wen, B.H. Ren, X. Wang, D. Luo, H.Z. Dou, Y. Zheng, R. Gao, J. Gostick, A. P. Yu, Z.W. Chen, Continuous CO_2 electrolysis using a CO_2 exsolution-induced flow cell, Nat. Energy 7 (2022) 978–988.

[73] Y. Hou, Y.L. Liang, P.C. Shi, Y.B. Huang, R. Cao, Atomically dispersed Ni species on N-doped carbon nanotubes for electroreduction of CO_2 with nearly 100% CO selectivity, Appl. Catal. B Environ. 271 (2020), 118929.

[74] Z. Zhao–Karger, P. Gao, T. Ebert, S. Klyatskaya, Z. Chen, M. Ruben, M. Fichtner, New organic electrode materials for ultrafast electrochemical energy storage, Adv. Mater. 31 (2019), 180659.